Advances in Environmental Technology 3 (2020) 173-189

Advances in Environmental Technology

journal homepage: http://aet.irost.ir

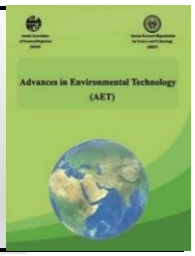

Vertically aligned carbon nanotube membrane: synthesis, characterization and application in salt water desalination

Hamed Azami[1*] Mohammad Reza Omidkhah[2]

[1] *Department of Chemical Engineering, University of Bojnord, Bojnord, Iran.*

[2]*Department of Chemical Engineering, Tarbiat Modares UniversityTehran, Iran.*

ARTICLE INFO

Article history:
Received 16 February 2021
Received in revised form
19 May 2021
Accepted 20 May 2021

Keywords:
Vertically aligned carbon nanotube membrane
Desalination
Reverse osmosis
Anti-bacterial membranes

ABSTRACT

Previous studies have used molecular dynamics simulation to assess the feasibility of applying vertically aligned carbon nanotube membranes (VA-CNT) for salt water desalination. The presented report experimentally determined the potential of salt water desalination by employing VA-CNT membranes. The VA-CNT membranes were synthesized through the template-assisted pyrolysis of polybenzimidazole-Kapton inside the pores of anodized aluminum oxide (AAO) and characterized by several techniques. The permeability, salt rejection, and biofouling tendency of VA-CNT membranes were measured in various operating conditions; the results were compared with the performance of a commercial reverse osmosis (RO) membrane (BW30). The VA-CNT membrane permeability was about twofold higher than the permeability of the RO membrane. Furthermore, the VA-CNT membranes had higher stability against biofouling phenomena; they also showed antibacterial activity so that about 70% of the adsorbed cells on the VA-CNT membranes were killed by CNTs tips that were vertically aligned on the membrane surface. The rejection efficiency of the VA-CNT membrane was comparable to that of the commercial RO membrane. Finally, the chlorine stability studies showed that high hypochlorite exposure (48000 ppm.h) did not significantly fail the flux and rejection of the VA-CNT membranes, confirming their chemical stability. This study shows the high capability of the VA-CNT membrane in the water treatment process.

1. Introduction

The worldwide water crisis has become one of the most serious international issues facing the global population [1-3]. Water treatment via membrane technology has been developed to mitigate the global water demand [٤]. However, membrane technology has some disadvantages. Most of the membrane processes, especially high pressure-driven membrane processes, are energy-intensive and are vulnerable to membrane fouling, which reduces membrane lifetime and performance [5,6]. The energy demand of membrane technology has declined over the past decade; yet, water treatment with membrane-based processes is still an energy consumptive technology. For instance, while the energy consumption of reverse osmosis (RO) process for the desalination of salt water decreased from 8.0 kWh/m^3 to 3.4 kWh/m^3, it is still higher than the theoretically required energy for desalination that is equal to 1.06 kWh/m3 [4,5]. Furthermore, membrane fouling, such as colloid fouling, organic fouling, and especially biofouling, deteriorates the membranes' performance resulting in high operating and maintenance costs [7-9]. Several strategies have been implemented to increase the membrane's permeability, thus reducing energy consumption and preventing membrane fouling [١٠].The modification of conventional polymer membrane properties is the main method to enhance the permeability and rejection efficiency of membranes. Nevertheless, this method is limited due to the 'trade-off' between the membranes' permeability and their selectivity [11, 12]. Another approach is to modify the surface of the membrane to be

*Corresponding author: Tel: +98-9122147625
Email address: h.azami@ub.ac.ir
DOI: 10.22104/AET.2020.4707.1281

smoother, more hydrophilic and fabricate anti-biofouling membranes [13,14]. Also, the application of antibiotics and antibacterial materials into the active layer of membranes has been studied [15-17]. Nowadays, a new generation of nanostructured membranes that incorporate nanotechnology into the membrane process has been proposed to overcome the disadvantages of membrane technology [18-20]. Amongst the various nanoparticles, carbon nanotubes (CNTs) have been extensively employed in membrane-based water treatment processes due to their unique properties, such as fast water transport and antibacterial activities. These features are required to synthesize a high-performance membrane with antifouling properties [21, 22]. CNT-based membranes are categorized into two general types: vertically aligned (VA) CNT membranes and composite (mixed) CNT membranes. Among the various types of CNT-based membranes, VA-CNT membranes have attracted the attention of scientists in many fields. Previous reports concerning VA-CNT membranes concentrated on the flow properties of fluids in CNTs [23-25]. There are various feasibility studies regarding VA-CNT membrane for the desalination of salt water by molecular dynamics (MD) simulation [26, 27]. The mean pore size of VA-CNT membranes considered in previous experimental studies was larger than 1 nm, which is higher than the hydrate ions of Na+ and Cl- [28, 29]. Therefore, the reported VA-CNT membrane cannot separate solute ions due to their large mean pore size and are insufficient for the desalination process. In this research, a template-assisted technique was applied to fabricate a VA-CNT membrane with a sub-nanometer mean pore size. The characterization of the VA-CNT membrane, such as its CNT structure and surface properties of the fabricated VA-CNT membranes, was measured by X-ray diffraction (XRD), Raman spectrometry, scanning electron microscopes (SEM) images, transmission electron microscopes (TEM) images, and air-water contact angle. The present study aimed to assess the performance of synthesized VA-CNT membranes in terms of permeability, salt rejection, and anti-biofouling activity. The results were compared with the performance of commercial RO membrane (BW30). The flux and rejection of the VA-CNT and RO membranes were evaluated by a lab-scale crossflow reverse osmosis system in various operating conditions. The anti-bacterial activity and anti-biofouling propensity of the membranes were studied in the next step. The presented study is the first to our knowledge that focuses on the synthesis of sub-nanometer VA-CNT membranes to desalinate seawater by investigating the operating condition and anti-biofouling affinity of VA-CNT membranes in the RO process. Further, the stability of the VA-CNT membrane to intensive chlorine exposure was not explored.

2. Materials and methods

2.1. Polymer preparation

The PBI and Kapton were chosen as sources of the pyrolytic carbon and were purchased from Aldrich Chemical Company Inc. (Aldrich, USA) and DuPont, respectively. The NMP was supplied by Merck (Merck, Germany) and used as the solvent for the polymer solutions. The polymer concentration was adjusted to 10% of PBI-Kapton (50%-50%) in the NMP solution. Equal quantities of PBI and Kapton were dissolved in NMP at 150°C. To avoid oxidation, inert nitrogen gas was used. Finally, the polymer solutions were filtered to remove any impurities.

2.2. Anodization of aluminum

The aluminum foils and all of the chemical solutions, including $HClO_4$, $H2SO_4$, H_3PO_4 (85%), HCl (37%), HNO_3 (67%), and NaOH, were from Merck (Merck, Germany). The other chemicals were of analytical grade. A two-step hard anodization (HA) process was applied to synthesize the anodic aluminum oxide (AAO). First, the aluminum foils were anodized under experimental conditions of 40 V, 0.3 mol/L oxalic acid concentrations, and 0 °C. The first step was performed for 1h. One hour of anodization is enough to make a protective barrier layer against the high voltages applied in the hard anodization step [30]. The anodization voltage was then increased to 130 V at a constant rate of 0.4 V/s. The hard anodization step was conducted for 3h at 130 V and 0 °C. The AAO strips were submerged in an $HCl/CuCl_2$ solution for 3h to remove the remaining aluminum and then immersed in phosphoric acid (5 wt. %) for 2h to obtain through-hole membranes.

2.3. Impregnation and pyrolysis

The pores of the AAO plates were immersed in 10% PBI and the Kapton solution (50/50). The soaking time was adjusted to 60 min for the impregnation of AAO. The templates were saturated by a polymer solution in this long impregnation time [٣١]. The impregnation step was followed by heat treating at 100°C for 1h. In the next step, the samples were pyrolyzed in flowing N_2 at 170 ml/min. The temperature was increased from room temperature to 800°C by stepwise heating protocol. The heating rates started from 10 °C/min and declined gradually by increasing the pyrolysis temperature to 4, 2, and 0.2°C/min. The dwell time at 800ºC was adjusted to 1h. The polymeric precursors were carbonized while sandwiched between two metallic disc meshes. The resultant carbon membranes were cooled slowly to room temperature. Figure S1 shows the thermal protocol of pyrolysis at a 170 ml/min N_2 flowing rate (See the supplementary materials). The impregnation and pyrolysis steps were repeated two time to synthesized double layer vertically aligned carbon nanotube (DVA-CNT) membranes.

2.4. Characterization of CNT membranes

The thermal properties of the polymer blend precursor and CNTs synthesized in AAO pores were studied using TGA. The maximum applied temperature in TGA analysis was 800°C. The TGA was conducted according to the pyrolysis procedure. Scanning electron microscopy analysis and Energy Dispersive X-Ray analysis were performed with an SEM microscope (TESCAN-Vega, Czech Republic) with an EDAX-CDU leap detector. The structure of the synthesized CNT into the AAOs was analyzed by TEM images taken by a Zeiss-EM900. Before inserting the sample grids into the microscope, the support was removed and the samples were sonicated in ethanol; then, they were dropped in the cupper grids and dried at room temperature. The Raman spectra and XRD patterns were taken by a Raman Image Spectrophotometer (Senterra, Bruker, Germany) and Phillips diffractometer (X'¬Pert MPD, Philips, Netherland), respectively, using Co-Kα radiation (λ= 0.1789 nm). Surface wettability was obtained using the sessile drop method, and the reported amounts of the CAs were averages of six measurements on each sample. In order to estimate the sub-nanometer pore size of the DVA-CNT membrane, a pore flow model by Sarbolouki and Miller [٣٢] was applied. The pore flow model involves the use of sieve statistics, which is based on the research of Pappenheimer et al. [٣٣], Ferry [٣٤], and Renkin [٣٥]. According to this model, the concentration ratio of the solute in the permeate stream to the feed stream decreases by a factor related to the ratio of solute diameter to mean pore size of the membrane. By assuming the plug flow velocity of the water into the pores of the membrane, the appropriate relationship is derived by Equation 1:

$$\frac{C_p}{C_f} = (1 - \frac{a_s}{r})^2 \quad (1)$$

where C_p and C_f are the concentration of solute in permeate and feed stream, respectively, a_s is the solute diameter, and r is the mean pore size of the membrane.

Equation 1 can be applied to relate the experimental salt rejection to the predicted pore radii given by:

$$r = \frac{a_s}{1 - (1 - R)^{0.5}} \quad (2)$$

In this equation, r refers to the pore size of the membranes, R is the experimental salt rejection, and a_s is the solute diameter.

2.5. Measurement of Antimicrobial Activity and anti-fouling potential of membranes

Antibacterial activities of the membranes were measured by the cultivation of aqueous suspensions of Escherichia coli (E. coli) on the membrane surface. The cell concentration of the culture was adjusted to 106 CFU/ml according to McFarland standards. All of the instruments and membranes were autoclaved before the experiments. The anti-bacterial activity of the membrane was evaluated by measuring the growth status of the adsorbed E. coli on the membranes according to the Wei et al. [٣٦] procedure with minor modifications. The 10 mm diameter membrane discs were selected. Ten µl of the aforementioned E. coli suspension was pipetted out on the membrane disc and cultivated in 37°C for 6 h. After the incubation step, the membranes were rinsed by 3 ml of normal saline solution (0.9% NaCl). The suspension was diluted several times, and 0.1 ml of the diluted suspension was spread completely onto a triplicate solid agar plate. The plates were sealed and incubated at 37 °C for 48 h. In the final step, the growth area of the viable cells on the agar plates was measured. The anti-bacterial ratio of the membranes was measured using the following equation:

$$R = \frac{B - A}{B} * 100 \quad (3)$$

where R is the anti-bacterial ratio, A is the area of viable colonies in contact with the membranes and are incubated on agar for 48 h, and B is the area of viable bacteria not in contact with the membranes but are incubated with the same procedure of the anti-bacterial characterization (blank control). The examination of the biofouling affinity of the CNT membranes and BW30 was conducted according to Xu et al. [37]. The anti-biofouling potential of the membranes and their performance were studied by measuring the water fluxes and salt rejections of the membranes after 48h of incubation of the membranes in the bacteria culture (20 mL of 106 CFU/ml of E. coli broth), using the method described in next section. The adsorption and growth of E. coli cells on the membrane surface after the permselectivity measurement were observed by SEM.

2.6. CNT and RO membranes performance

The membrane pour water permeability of the DVA-CNT and RO membranes was evaluated in the cross-flow membrane filtration system pressurized with a high-pressure pump (Figure S2, Supplementary Information). The flux of the DVA-CNT membranes was investigated by measuring their permeate volume after 2h of filtration, and the results were compared with the commercial RO membrane (BW30). The distilled water, selected as the feed stream and trans-membrane pressure of the experiments, was adjusted to 10, 20, 30, 40, and 50 bar to investigate the impact of operating pressure on the performance of the membranes. The enhancement factor (E) is the ratio of the measured flux to the no-slip flux calculated by the Hagen–Poiseuille equation and was calculated by Equations 4 and 5 [٢٥] This factor indicates the magnitude of the increased flux of DVA-CNT membranes from no-slip condition fluid flow.

$$E = \frac{Q_{measured}}{Q_{No-slip\ (HP)}} \quad (4)$$

$$J_{HP} = \frac{\pi r_p^4 \Delta P}{8\mu\tau L} \quad (5)$$

where J_{HP} is the fluid flow calculated from the Hagen-Poiseuille equation, and r_P is the radius of the nanotube.

Moreover, the permeate flux of the membranes under various applied transmembrane pressures (TMP) and salt concentrations was measured to investigate whether the DVA-CNT membrane could be applied in future RO processes. The trans-membrane pressure ranged from 10 to 40 bar, and 2000 ppm to 40000 ppm was selected for the feed salt concentration. The concentration of the NaCl solution in the permeate stream was measured by a water quality tester (99720, MIC, Taiwan). The rejection efficiency was calculated by Eq. (6):

$$R = \left(1 - \frac{C_p}{C_f}\right) \times 100 \quad (6)$$

where C_p is the permeate concentration and C_f is the feed concentration.

3. Results and discussion

3.1. Synthesis and characterization of VA-CNT membranes

The structure of the AAO template is characterized as a close-packed hexagonal arrangement of cylindrical nanopores vertically aligned to the surface of the membrane (Figure S3, Supplementary Information). The AAOs that were synthesized through the hard anodization process had asymmetric structures. The template had an active top layer produced through the mild anodization step. As shown in the Supplementary materials (Figure S3 (A)), the active layer had a mean pore size of 24 nm (See the supplementary information). The other main parameter of the active layer was its, thickness, which was almost 430 nm (Figure S3 (C)). The active layer was on top of the underlying substrate alumina synthesized through the hard anodization step. The substrate layer acted as a support of the active layer and provided the mechanical stability of the AAO template. It had a mean pore size of 128 nm and had minor hydraulic resistance against water flow through the membrane. The properties of the AAO template are summarized in Table 1.

TGA is a useful technique to analyze the transformation of a polymers structure to a graphite network by the thermal process. It is measured to find the optimum temperature of the template-assisted pyrolysis of PBI-Kapton to synthesize VA-CNT membranes. Figure S4 shows the TGA results of a CNTs/AAO membrane. Figure S4 shows that about 90% of the weight loss of the polymer solution occurs at up to 600 ºC. Above 600ºC, the resulted carbon structure went through the plateauing trend, and only the arrangement of the carbon structure improved. Consequently, in the final pyrolysis temperature of 800°C, all of the organic matter was transformed into the carbon structure. The pyrolysis of PBI-Kapton into the pores of the AAO contributed to the transformation of a polymer solution into the carbon structure that covered the wall of the pores in the AAO network [۳8]. The AAO templates showed high thermal stability and remained intact after heat treatment at 800°C. At this temperature, the pore wall of AAO was covered by a carbon layer while all of the pores were open. Figure 1 shows the surface and cross-section of the CNT membranes synthesized at 800°C. The organic fraction of polymers covered the pore walls and also the surface of the AAO templates so that the mean pore size of the CNT membrane was reduced to about 8 nm in the VA-CNT membranes. As can be seen in Figure 1A, the VA-CNT membrane had uniform pore size distribution. The thickness of the CNTs synthesized into the pores of AAO was proportional to the polymer content, so that the polymer blend attached to the pores wall and gradually transformed to the carbon structure [۳8]. Consequently, the DVA-CNT membrane had a microporous structure active layer, and the mean pore size distribution of DVA-CNT membrane was a sub-nanometer.

Table 1. The properties of the AAO template synthesized through the HA anodization process.

Active Layer			Support layer		
Mean pore size (nm)	**Thickness (nm)**	**Pore density (#/cm²)**	**Mean pore size (nm)**	**Thickness (µm)**	**Pore density (#/cm²)**
24	430	2.86×10^{10}	128	100	4.25×10^{8}

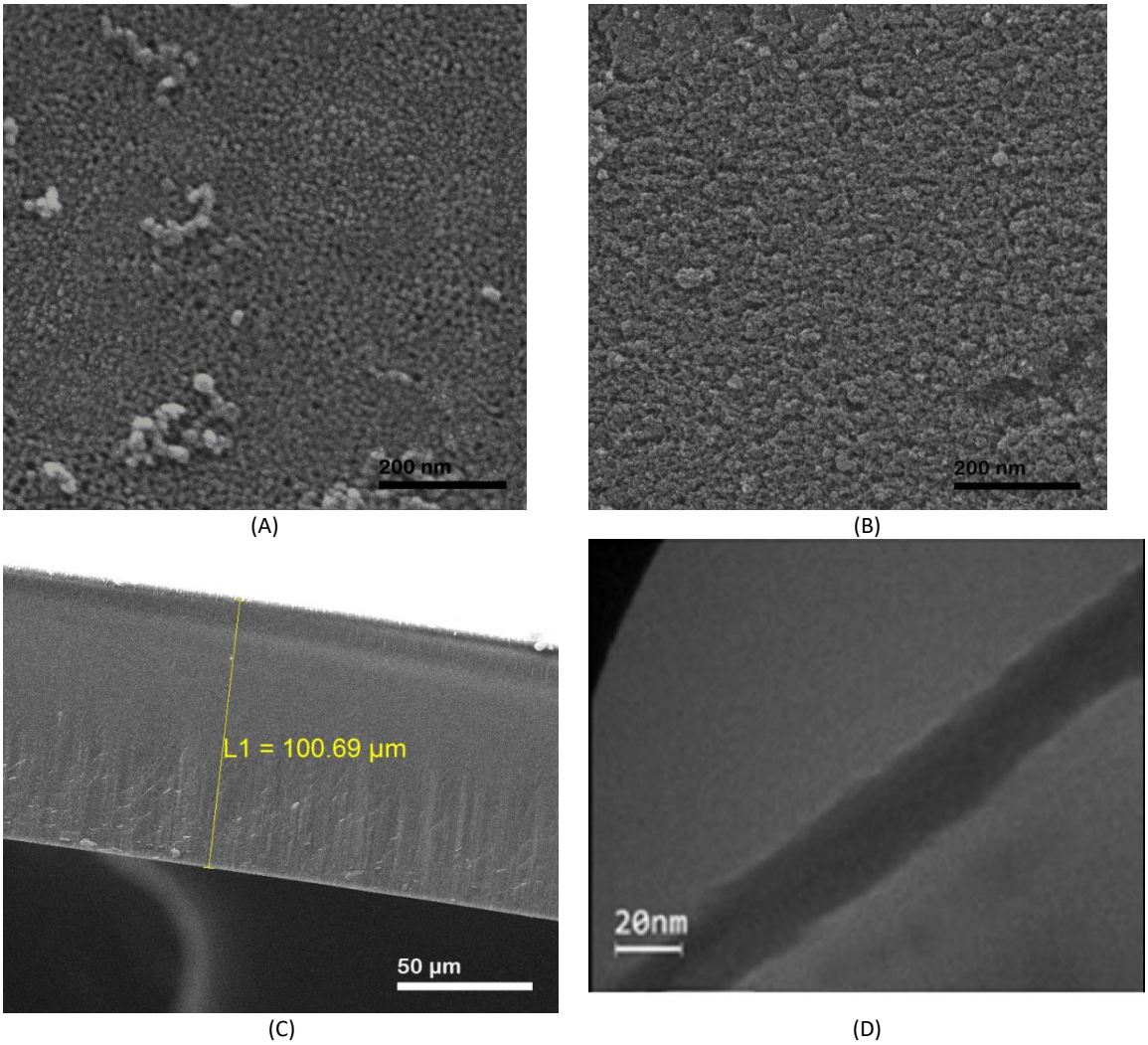

(A) (B) (C) (D)

Fig. 1. Surface images of VA-CNT membrane (A), DVA-CNT membrane (B), cross section of CNT membranes (C), and TEM image of MWCNT synthesized by two-step pyrolysis process (D).

The outer diameter of the CNTs was equal to the mean pore size of the AAO templates, which was 24 nm. The inner diameter of the CNTs in the VA-CNT membranes was 8 nm and equal to the mean pore size of the VA-CNT membranes. A dense carbon layer covered the surface of the DVA-CNT membranes so that the mean pore size of the DVA-CNT membrane, which was equal to the inner diameter of CNTs, was sub-nanometer and not detectable by SEM image analysis. The TEM image of the CNTs, synthesized via two-step template-assisted pyrolysis, revealed they had a uniform structure (Figure 1D). The mean pore size of the DVA-CNT was measured by the salt rejection efficiency of the DVA-CNT membrane, as discussed later. All of the CNTs were about 430 nm long and equal to the active layer of the templates. The elemental analysis of the CNT membranes obtained by EDX is shown in Table 2. The elemental analysis showed that the PBI-Kapton structure decomposed, and only its carbon fraction remained after the pyrolysis process. The carbon fraction in the DVA-CNT membranes was about 50% higher than its fraction in the VA-CNT membranes, which was a consequence of a second layer of carbon layer made through the second pyrolysis step. The Raman spectroscopy and XRD patterns analysis are indicative ways to clearly show the formation of the carbon phase into the AAO pores and its structure.

Table 2. Raman spectra analysis, XRD, and elemental analysis of the VA-CNT and DVA-CNT membranes.

Sample	AL	O	H	C	N	G position (cm^{-1})	D position (cm^{-1})	I_G/I_D	2θ d_{002} (º)	d_{002} (Å)	2θ d_{100} (º)	d_{100} (Å)
VA-CNT	48	45	0	7	0	1615	1310	0.91	32.05	3.24	55.33	1.93
DVA-CNT	46	43	0	11	0	1592	1294.5	0.99	35.33	2.95	55.5	1.92

The XRD spectra of the CNT membranes are presented in the Supplementary documents (Figure S5). It shows two characteristic graphitic peaks: a broad diffraction peak at about 30-35° (002) and a low intensity peak almost at 55 (100), which represent the interlayer spacing of the different graphite layers of multiwall carbon nanotubes and the carbon-carbon bond in structure of carbon network, respectively. The value of the interplanar spaces (d002) and carbon-carbon bond in the carbon plane (d100) of VA-CNT and DVA-CNT membranes are indicated in Table 2. Generally, an increase in the crystallinity of the carbon nanotubes is revealed in lower values of d002 [٣٩]. The investigation of the XRD pattern showed that the samples had a graphitic structure. The d002 of the synthesized VA-CNTs and DVA-CNTs were lower than the graphite structure (d002= 3.35 Å), which indicated that they were more compact than graphite. The XRD pattern of the DVA-CNTs had a sharp d002 peak at 2θ= 35.33°. Compared to VA-CNTs, DVA-CNTs were more compact and had a crystalline carbon network as indicated by its intense XRD peak that occurred at a higher 2θ position (2θ = 35.33°). It seems like the second pyrolysis step acted as a post-treatment process, allowing the CNTs of the VA-CNTs' membrane to rearrange into the AAO pores. Consequently, a defect in the carbon network of the VA-CNTs membrane mitigated through the second step pyrolysis, and the DVA-CNTs membrane had a more crystalline carbon structure. In our previous work, we synthesized the carbon molecular sieve membrane through the pyrolysis of PBI-Kapton in a free environment [٤٠]. A comparison of the network structure of the carbon molecular sieve membranes, VA-CNTs, and DVA-CNTs showed that the CNT membranes, especially the DVA-CNT membrane, were more uniform and had an ordered graphitic structure. We attributed the improvement in the crystallinity of the carbon nanotubes to the impact of the confined environment of the PBI-Kapton pyrolysis process in nanopores of the AAOs. It was shown that several intrinsic properties of the pyrolytic materials were changed by finite-size effects [٤١], and the crystallinity of the pyrolyzed carbon in the restricted condition was higher than the carbons synthesized through the pyrolysis process in a free environment [٤٢]. The Raman spectra of CNTs display the two characteristic bands of the disordered carbon structures. The first one is at about 1600 cm^{-1} (the G-line) and stands for the graphite structure; the other one is a peak at 1300 cm^{-1} (called the D-line), which is an indication of disorder fraction of carbon materials [43-45]. The relative intensities of both the G and D lines (IG/ID) show the quality of crystallinity of the carbon network. In general, a higher IG/ID ratio coincides with a higher degree of crystallinity. The Raman spectra of the synthesized CNT membranes are shown in Figure S6 in the Supplementary content. The position of the G and D bands and the ratio of these intensities (IG/ID) are shown in Table 2. Due to the greater carbon fraction in DVA-CNTs, their Raman pattern had higher intensity. The IG/ID ratio of DVA-CNTs exceeded 0.99; however, its value in VA-CNTs was restricted to 0.9, which showed the 10% enhancement in the crystallinity of the CNTs synthesized through two-step pyrolysis. This improvement in the alignment and crystallinity of the CNTs through the second pyrolysis step is in agreement with the XRD analysis results. The XRD and Raman analysis of the CNTs synthesized into the AAO pores through the pyrolysis of PBI-Kapton resulted in the following conclusions. The carbon nanotubes were formed with a high degree of compactness and crystallinity since their interplanar space (d002) was lower than the interplanar space between the carbon sheets in the ideal graphite (d = 3.35 Å). The IG/ID ratios of the VA-CNTs and DVA-CNTs membrane were also higher than its amount observed in the carbon black structure, which was 0.39 [٤٦]. The crystallinity of the CNTs synthesized through the template-assisted pyrolysis into the pores of the AAOs was the same as the commercial MWCNTs [47,48]. Also, the DVA-CNTs were more ordered because the second pyrolysis step acted as a post treatment process. These results revealed that the vertically aligned carbon nanotubes synthesized in the present research had a higher crystallinity degree than the graphitic carbon structures obtained from organic materials pyrolyzed in a free environment.

3.2. Pure water permeability of the DVA-CNT and RO membranes

The performance of the DVA-CNT and BW30 membranes was evaluated by a cross-flow reverse osmosis setup. The VA-CNT membrane is not appropriate in desalination due to its 8 nm mean pore size and is no longer considered in this work. Figure 2 shows the pour water flux of the DVA-CNT and RO membranes under various applied pressures and temperatures. These figures show that the pure water permeability, Lp, increases in higher temperatures. It is expected since the viscosity of the water declines in higher temperatures. The water permeability of the membrane and kinematic viscosity relation are inversely proportional [٤٩]. Consequently, the increase in operating temperature causes increments of water flux of the membranes. Moreover, based on the Arrhenius equation, previous research has shown that there is a linear relation between Ln (Lp) and 1/T [٥٠].

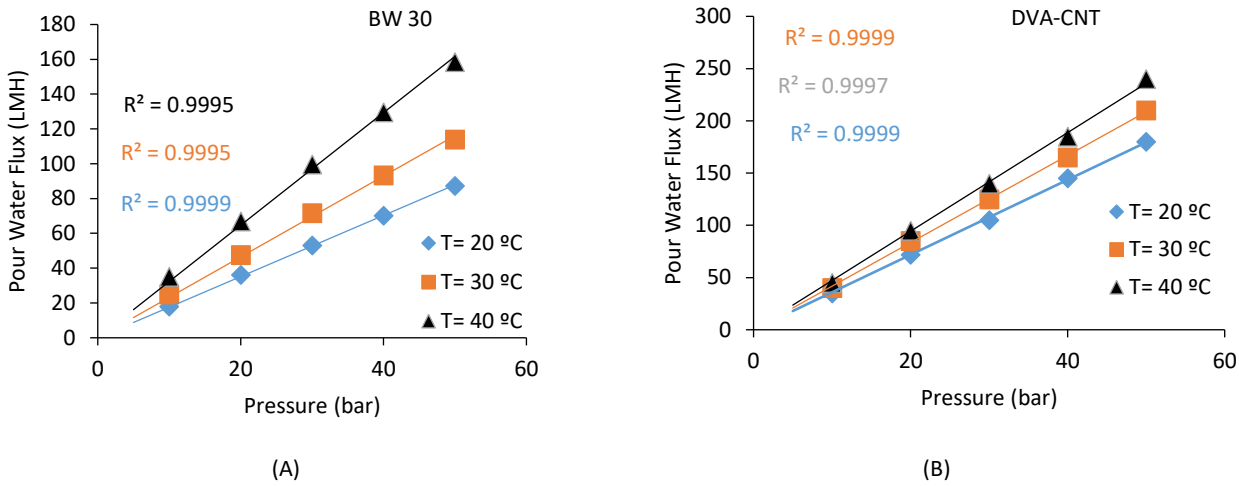

(A) (B)

Fig. 2. Pour water permeability of commercial RO membranes (A) and DVA-CNT membranes (B) in various temperatures versus the trans-membrane pressure.

The flux of both membranes had a linear relation via transmembrane pressure. The linear relation indicated that the permeability of the membranes was constant in applied transmembrane pressure. In Figure 2 (A & B), the DVA-CNT membranes show water flux about twofold of the commercial RO membranes. Previous studies indicate that the VA-CNTs membranes show higher permeability in comparison to commercial polymeric membranes with the same structure [٥١]. High flow velocities of water molecules through CNTs were expected due to the nearly frictionless nature of the water flow into the CNTs with minimal scattering or chemical attraction [٥٢]. Joseph and Aluru showed that a unique combination of features such as the frictionless and hexagonal structure of the CNTs' inner wall, OH bond orientations of water molecules, and hydrogen bonding in the depletion region had a direct impact on the enhancement of flow rates [٥٣]. In all the models and observations, the atomically smooth structure of the graphite surface, intrinsic to the CNTs microstructure, makes it accessible to reach the enhanced flow as much as a 3-4 order of magnitude of theoretical flow in porous media [٢٤].

3.3. Performances of the DVA-CNT and RO membrane

The water fluxes and salt rejections for the membranes as a function of NaCl concentrations (2000, 10000, 25000, and 40000 ppm) at 20, 30, and 40 bar are presented in Figure 3. In general, it can be seen that the water flux declined by an increase in solute concentration or decrease in operating pressure. In addition, there was a major increment in water fluxes for the DVA-CNT membrane compared to commercial BW30. These results also followed the trends observed with pour water results. The salt concentration greatly affected the performance of the membranes, particularly in BW30. For instance, the BW30 membrane showed a significant decrease in salt rejection from 99% to 49% as the salt concentration was raised from 2000 to 40000 ppm, respectively. The loss of performance of the BW30 membrane is comparable to the results reported for the polymeric membranes [٥٤], related to an increase in the concentration gradient between the two sides of the membrane leading to higher solute diffusion through the membranes. On the other hand, Fornasiero et al. indicated that If electrostatic interactions at the membranes' surface play a role in ion rejection, then the rejection efficiency of the membrane was highly sensitive to solution ionic strength, and an increase in ionic strength resulted in the worsening of membrane rejection [٥٥]. Furthermore, osmotic pressure is a function of the concentration of salts in the feed water. As the concentration of ions increases, so does the osmotic pressure of feed the stream, and consequently, the net driving pressure decreases. The permeate flux of the membrane is proportional to the driving pressure of the feed stream [٥٦]. While, the DVA-CNTs' membrane showed a higher rejection efficiency due to efficient molecular sieve phenomena conducted by the inner diameter of DVA-CNTs. Previous studies indicated that inorganic molecular sieve membranes had high stability against salt concentration fluctuation [٥٧]. In fact, the high water flux coupled with reasonable and stable salt rejection (near 90%) suggests that the DVA-CNTs membrane structure did not form preferential pathways for the transport of saline water.

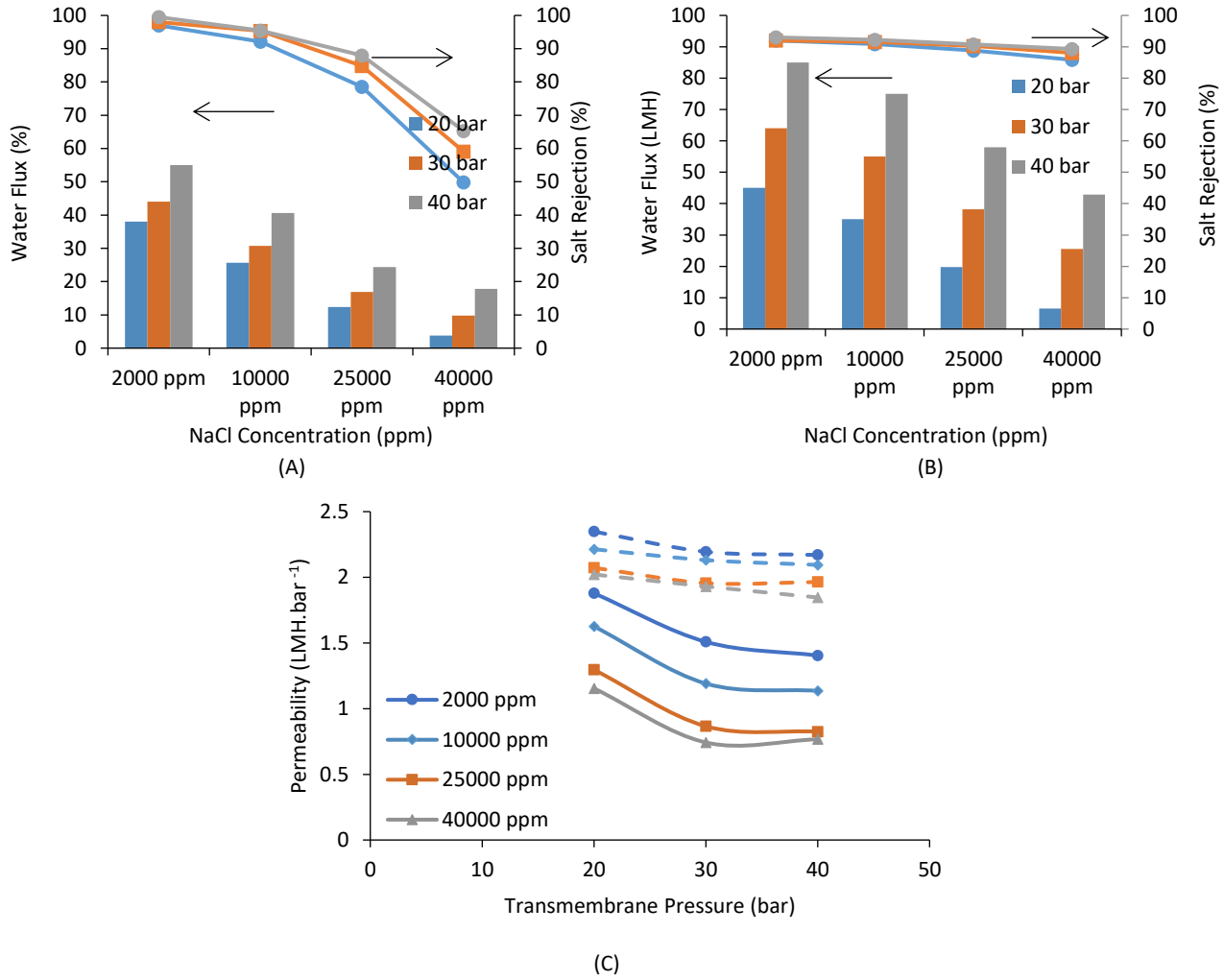

Fig. 3. Water flux properties and salt rejection of the BW30 (RO) membrane (A) compared to DVA-CNT membrane (B) in various salt concentration and transmembrane pressure of 20, 30 and 40 bar, water permeability, Lp, of DVA-CNT (dashed line) and BW30 (solid line) membranes (C).

BW30 and DVA-CNT membranes were applied in order to investigate the effect of pressure on the permeation properties of NaCl solutions, as presented in Figure 3. The rejection of NaCl increased with the increment of operating pressure for both membranes. The increased rejection with increased operating pressure is a usual trend in reverse osmosis processes [58]. As mentioned above, the water flux of the membranes increased proportionately with the applied transmembrane pressure, while the solute flux was independent of the operating pressure.

Despite the water flux of the BW30 membrane raised in higher transmembrane pressure, the water permeability of the BW30 decreased almost 30% by an increase in hydraulic pressure from 20 bar to 40 bar (Figure 3(C)). Whereas, the permeability of the DVA-CNT membranes remained nearly constant and equal to 2.08±0.14 (LMH.bar^{-1}). This indicated that polymeric BW30 membrane compacted in higher hydraulic pressure, which is an inherent disadvantage of polymeric membranes [59] and lost its permeability; however, the DAV-CNT membrane had a robust mechanical strength, and its structure remained intact in high operating pressure.

Generally, the state of water molecules and their transport mechanism are unclear if they are penetrating through sub-nanometer micropores. In this case, the nearly constant Lp indicates that Δp is the only driving force for water permeation through DVA-CNT membranes, approving that the water permeated through DVA-CNT membranes is in the liquid state.

The solute rejection and flux of the DVA-CNT membrane improved with an increase in the applied pressure, which was also observed in previous studies on inorganic molecular sieve membranes [60-61]. The rejection efficiency of the ions in NF and RO is conducted by the charge repulsion effect and the sieving phenomena. If the surface charge plays a major role, an increase in the feed concentration should lead to a major drop in salt rejection due to the reduction of charge repulsion, which is often observed for many polymeric NF and RO membranes. In this study, the rejection of NaCl by the BW30 dropped

significantly by an increase in the salt concentration of the feed, which indicated the impact of the reduction of the surface charge repulsion. The mechanism of rejection of the DVA-CNT membrane was mainly based on size exclusion and molecular sieving because they had high rejection efficiency in all solute concentrations. The mean rejection efficiency of the DVA-CNT membrane was equal to 90.39 ± 1.97 % over the feed concentration (2000 - 40000 ppm). Xu et al. [62] showed that the NaCl permeability had a slight variation by feed concentration, which approved the minor impact of the surface charge on the interaction between ions and the pores of a molecular sieve membrane on the rejection capability of molecular sieve membranes.

The pore size of the DVA-CNT membrane was measured by the pore flow model proposed by Sarbolouki and Miller [32]. The solute diameter of salt (a_s) was determined by Gierer's [63] relation, which is a modified Stokes-Einstein equation for solutes with comparable size to the solvent. According to the Gierer equation, the size of water and NaCl were 1.5 Å and 2.4 Å, respectively. Assuming that the rejection efficiency of the DVA-CNT membrane was 90.38, the mean pore size of the DVA-CNTs was about 3.4 Å. The pore size of the DVA-CNTs was also predicted by the equation below proposed by Recum [64], which was equal to 3.2 Å and had a good agreement to the value obtained by the pore flow model.

$$PS=V(M\_w/2.2) \quad (7)$$

where PS is mean pore size of the membrane (Å) and Mw is the molecular weight of the solute rejected by the membrane (g/mol). Thomas et al. proposed six mechanisms to elucidate salt rejection in nanoporous membranes comprising CNTs membranes [65]:

1. Size exclusion of bare ions,
2. Dehydration effects (size exclusion of the hydration shell and reduction of ion coordination numbers),
3. Entropic differences of ions when they are entering into the CNTs,
4. Charge repulsion,
5. Subtler effects involving interactions of various ions with
the pore that usually occurs in biological channels,
6. Interactions of solutes and functional chemical structures of the pore entrance.

Among these mechanisms, steric exclusion of bare ions and their hydration shells via narrow pristine nanotubes are widely considered the mechanistic basis of mechanisms for salt rejection in RO processes [66,67]. The third mechanism involves entropic differences through the CNTs. Sub-nanometer nanopores can also reject salt by limiting the number of solutes geometric arrangements to distinct physical configurations in which salt ions can successfully enter the nanopores [68].

The fourth mechanism occurs in functionalized CNT membranes according to Donnan exclusion theory that describes the rejection mechanism and behavior across charged membranes. The fifth and sixth mechanisms mentioned by Thomas et al. refer to phenomena that occur as a consequence of the overall nanopore morphology and particular chemical structures within the nanopore. These mechanisms play an important role in biological membranes.

MD simulations [69,70] reveal that if the nanotube is uncharged, the completely steric exclusion of small ionic species such as Na^+ and Cl^- requires CNTs with inner diameters of about 0.4 nm. This pore size is smaller than the size of the hydrated ions (dk Cl−= 6.6 Å and dk Na+= 7.2 Å) [71,72]. At this scale, the ions should lose a portion of their hydration shell and coordination numbers to enter the CNTs, showing a very high energy barrier to penetrate ions through the membrane (approximately140 kJ/mole). However, there is a low free energy barrier to water conduction in sub-nanometer CNTs, and its energy barrier is less than 1.67 kJ/mol [73,74]. The small free energy barrier outside the tip of the tube occurs due to the intense van der Waals interactions of the oxygen and carbon atoms arranging the molecules near the nanotube-water interface that has been depicted before [75]. Cory's research group investigated the desalination potential of a VA-CNT membrane according to the size of the nanotubes [26,76]. They found that as the inner diameter of nanotubes increased from 0.32 nm to 0.49 nm, and then to 0.59 nm and 0.75 nm, the salt rejection ability of the CNT membrane deteriorated to 100%, 100%, 95%, and 58%, respectively.

Based on the results of the aforementioned MD simulations, the salt rejection efficiency of the DVA-CNT membrane within 0.34 nm mean pore size should be equal to 100%. However, it is noteworthy that in order to attain high salt rejection, the pore size distribution of the CNT membrane must be precisely narrowed, and any fluctuation in the pore size distribution deteriorates the salt rejection [77]. As a rough estimation, to achieve reasonable salt rejection (>95%), it is essential that less than 1% of the CNTs have a diameter larger than 5.9 Å (CNT (7, 7)), which is complicated and remains a substantial challenge [26]. It seems that there were few MWCNTs in the DVA-CNT membrane with an inner diameter larger than 5.9 Å that reduced the salt rejection to about 90%.

3.4. Enhancement factor of water flow through DVA-CNT membranes

The flow rates of water through the CNT based membranes are two to five orders of magnitude greater than those predicted by the no-slip Hagen Poiseuille relation [24,25]. The atomically smooth and non-wetting structure of CNTs implies that the flow rate enhancement is based on liquid slip at the water/carbon interface. Hummer et al., using MD simulation [78], suggested that the enhanced flow was related to the sub-continuum, single-file molecular transport phenomenon. Cory's research group showed that

the ability of rapidly transport liquids in the carbon nanotube membranes based on no hydrophobic/hydrophilic interaction of water molecules into the CNTs membrane and hydrophilic modification of the CNTs caused a drastic reduction of water flow [79]. The pour water flow enhancement factors of the DVA-CNT membrane are shown in Figure 4. The mean enhancement factor of the DVA-CNT membrane changed from 2.84× 〖10〗 ^3, 2.63× 〖10〗 ^3, and 2.44× 〖10〗 ^3 as the operating temperature increased from 20°C to 30°C and 40°C, respectively. In contrast, the enhancement factor was independent of the operating pressure. As previously mentioned, the enhancement factor (E) represents the ratio of the increased water flux in comparison to the water flux in a conventional no-slip condition. Since both the empirical flux and theoretical flux have a linear relation with the operating pressure, their ratio is independent of pressure. As shown in Figure 4, the enhancement factor of the DVA-CNT membrane decreases by increasing operating temperature. The observed trend is based on the fact that an increase in water temperature causes the increment of entropy of water molecules, which might disrupt the water transport through CNTs. Moreover, a previous report indicated that the relative viscosity of the confined water molecules within the CNTs increased at higher temperatures [80]. Previous researches observed this high enhancement factor on the DVA-CNT membrane. Holt's research group synthesized a sub-2-nanometer VA-CNT, which had an enhancement factor equal to 3000± 1700 [25]. However, Yoon's group synthesized a high permeable VA-CNT membrane with an enhancement factor as high as 69039 [51], and the VA-CNT membrane in Hinds' group had an enhancement factor of 61,403 [23,24]. The higher enchantment factor of the VA-CNT membrane synthesized by Hinds and Yoon was based on the larger mean pore size of their membrane that was 6±2 nm and 4.8±0.9 nm, respectively. Fast water flux is described as hydrophilic water quickly passing through the hydrophobic CNT's inner wall due to low hydrophilic-hydrophobic interaction [78], which has been previously revealed by many researchers [53,81] . Furthermore, it seems that water molecules spontaneously flow into the internal CNTs by forming a strong hydrogen-bonding network, which is a thermodynamically stable arrangement of water molecules within the interior of CNTs [75,82].

3.5. Antibacterial properties of the DVA-CNT and BW30 membranes

The antibacterial efficiency of the BW30 and DVA-CNT membranes were evaluated against Gram-negative E. coli. E. coli is one of the widespread bacteria in water and wastewater resources. It is an appropriate reference bacteria to assess the anti-bacterial activity of various materials. The antibacterial efficiency of the membranes is summarized in Table 3. In contrast to the low antibacterial activity of the commercial BW30 membrane, the DVA-CNT membranes had an antibacterial surface that killed about 70% of the viable cells deposited on its surface. The mechanism of the antibacterial activity of the CNTs could be explained by the physical contact and interaction between the E. coli and CNT membranes surface. These included the physical adsorption of viable cells, inhibition of bacterial growth by impairing the respiratory chain, formation of cell-CNT aggregates, and penetrating the CNTs into the cell membrane. Consequently, it led to the dispersion of intracellular constituents of the bacteria and the death of viable cells due to the disruption of the cell membrane [83].

Table 3. Antibacterial efficiency of the CNT/AAO sheets.

Sample	Antibacterial efficiency (%)	Contact angle (°)
BW30	15%	55±1.2
DVA-CNT	70%	85±2.43

Previous reports indicated that CNTs have anti-microbial properties [84]. In another study, Elimelech's group revealed that CNTs had a high aspect ratio and penetrated into the cellular membranes to destroy their structures and disrupt the cells [85]. The first step of bio-interactions of the cells and membrane surface is based on the surface properties of the membranes so that more hydrophobic surfaces have more tendency to adsorb microorganisms [38,86]. As measured by air-water contact angle analysis, the hydrophobicity of the membranes is shown in Table 3. The DVA-CNT membranes were more hydrophobic than the BW30, and consequently, more prone to adsorb the viable cells. Additionally, the higher hydrophobicity of the DVA-CNT membrane caused the strong attachment and aggregation of cells followed by penetrating the CNTs cap into the cells' membrane and the disruption of cells. As the previous report indicated, due to their smaller nanotube diameter, direct cell contact with CNTs deteriorated the cellular membrane integrity and morphology of E. coli [87].

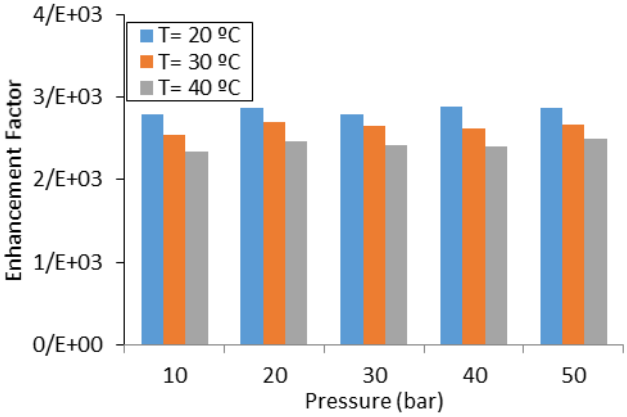

Fig. 4. Enhancement factor of DVA-CNT membranes in various temperatures versus the transmembrane pressure.

3.6. Membrane biofouling tendency

Figure 5 shows the variation of relative permeate flux and solute rejection of the BW30 and DVA-CNT membranes

after the biofouling occurrence in a lab-scale cross-flow system under identical operating conditions of the unfouled membranes. Despite that the rejection deteriorated in both membranes, no bacteria were detected in permeates of the DVA-CNT membrane and RO membrane. After E. coli culturing, the water flux of the fouled membranes and also their salt rejection decreased significantly compared to pristine membranes. The reduction in membrane permeability and salt rejection after biofouling can be described as follows. Once the biofilm formed during the biofouling phenomena, the new barrier layer against the water permeation across the membrane was added to the total hydraulic resistance of the membranes, giving rise to an obviously decreased membrane water flux. Moreover, the biofilm inhibited the back diffusion of salt ions and changed the cross-flow hydrodynamics via an increase of the hydrodynamic boundary layer on the membrane surface, resulting in enhanced concentration polarization [88,89]. The greater ionic activity in the boundary layer caused the increment of salt transport through the membrane, and thus, the salt rejection decreased after the biofilm formation. In addition, the polymeric membranes were vulnerable to biodegradation or biodeterioration via enzymes, localized pH, or changes in redox potential [90]. It could be another reason for the fall of salt rejection in the BW30 membrane.

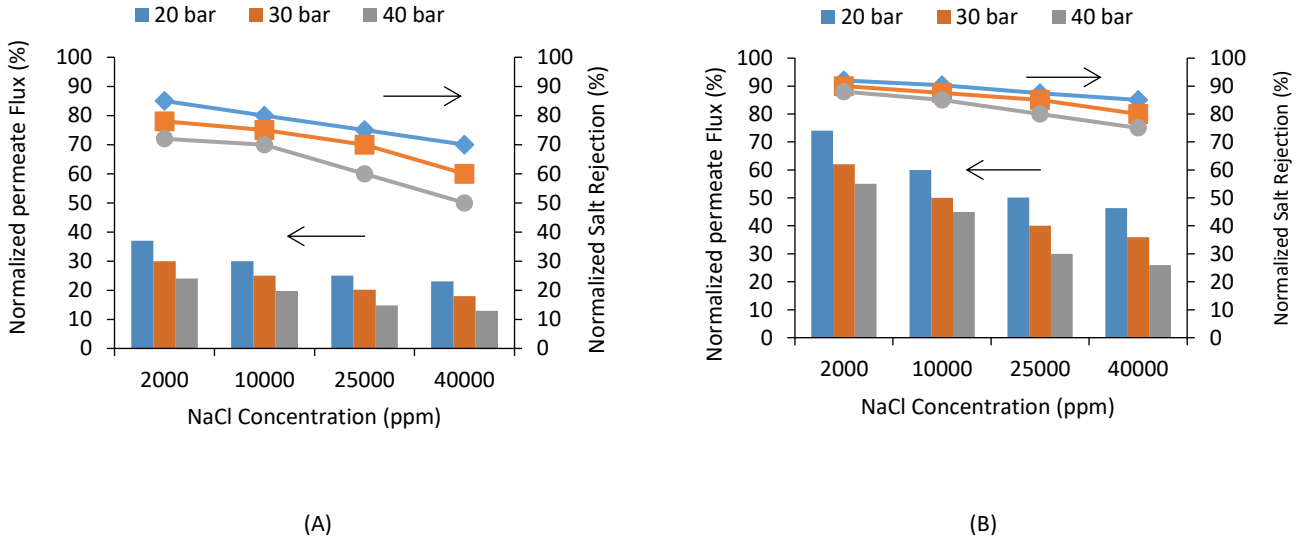

Fig. 1. Normalized permeate flux reduction and rejection efficiency of the RO membrane (A) and DVA-CNT membrane (B) after biofouling step.

The previous study indicated that the more hydrophobic membrane surface would result in more membrane fouling [14]. Thus, it was expected that severe biofouling would occur in the DVA-CNTs' membrane since its membranes were more hydrophobic than the BW30 membrane (Table 3). However, contrary to this expectation, the biofouling phenomena on the DVA-CNT membrane had a minor impact on membrane performance, as shown in Figure 5. The reduction of permeate flux in the RO membrane (65-85 %) was more than that in the DVA-CNT membrane (25-75%). Furthermore, fewer bacterial colonies were observed on the DVA-CNT membrane surface than on the RO membrane surface, as shown in Figure 6. The explanation of this phenomenon can be found in the antimicrobial activity of CNTs: they vertically align on the surface of the CNT membrane. Previous reports point out that CNTs act as “nano darts”; they attach and penetrate into the cells, disturb their metabolic activities, and kill the bacteria [91,92]. Consequently, the bacteria might be inactivated or killed by physical damage or oxidative stress, then detach from the DVA-CNT membrane surface, which leads to less biofouling occurring on the CNT membranes [93-95]. The surface morphology of the RO and DVA-CNT membranes after biofouling were observed by SEM. As shown in Figure 6, there are large numbers of E. coli bacteria adsorbed on the commercial polymeric membrane surface. Since the SEM analysis was conducted after examining the fouled membranes performance, the residual E. coli cell on the membrane indicated that the cells attached firmly to the surface of membranes and were hard to detach by cross-flow agitation. However, only a few E. coli cells were detected on the CNT membrane surface, indicating that the CNT membrane could provide the membrane with an excellent anti-biofouling property. Compared with the RO membrane, the lower deterioration occurred on the performance of the DVA-CNT membrane after culturing for 48 h. It pointed out that the DVA-CNTs membrane had great potential in desalination processes due to its reasonable performance and resistance to biofouling.

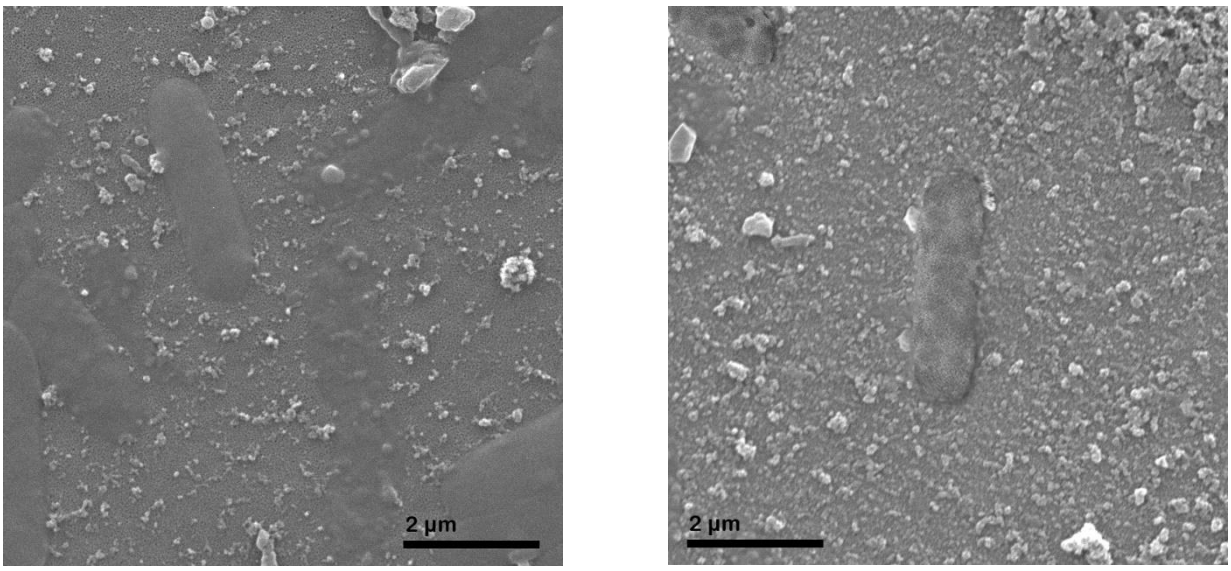

(A) (B)

Fig. 6. SEM images after biofouling occurrence after 48h incubation of membranes in bacteria culture (A) BW30 RO membrane and (B) DVA-CNT membrane.

3.7. Effect of hypochlorite exposure on desalination performance of DVA-CNT membranes

Various studies on RO membranes reveal that biofouling is the major cause of RO membrane failure [37,89,96]. Chlorine is a practical chemical agent to mitigate membrane biofouling in water treatment processes. However, free chlorine is an intensive oxidizer and commercial aromatic polyamide TFC; RO membranes are vulnerable to free chlorine [97]. The residue free chlorine in the feed stream destroys the structure of polyamide RO membranes and causes membrane failure, as evaluated by the deterioration of separation performance [98,99]. Consequently, an experiment was conducted to assess if the DVA-CNT membranes could withstand exposure to concentrated free chlorine. The DVA-CNT membranes were immersed in the 1000 ppm sodium hypochlorite solution for two days (48,000 ppm.h); then, the performance of the chlorinated DVA-CNT membranes was measured at the same operating conditions of section (3.3). Figure 7 shows the performance of the chlorinated DVA-CNT membrane in comparison to the pristine DVA-CNT membrane. The permeability of the chlorinated DVA-CNT membrane was reduced, whereas its rejection efficiency improved. It seems that the chlorine exposure caused some changes in the DVA-CNT membranes. Sodium hypochlorite (NaOCl) is an oxidizing agent that can change the structure of CNTs [100]. It seems that during the hypochlorite contact, NaOCl oxidizes the CNTs tip and is introduced into the MWCNTs interlayer [101]. The functionalized DVA-CNT membrane is characterized by FT-IR spectra (Figure 8). There are two peeks around 1120 cm^{-1} and 970 cm^{-1} related to the C–O bonds, which are found in the phenolic groups [102]. The peak at 1560 cm^{-1} is attributed to aromatic ring stretching or the presence of a highly conjugated C=O group. A peak at 2320 cm^{-1} is assigned to -OH stretching bond from strong H bond in Carboxylic function. The peak at 3422 cm^{-1} is associated with the –OH stretching vibration from COOH groups [100]. The existence of oxygen-containing groups on the DVA-CNT membranes confirms that the oxidation phenomena occurs during the chlorination step, which is in agreement with the results obtained from the chemical oxidation of CNTs [103].

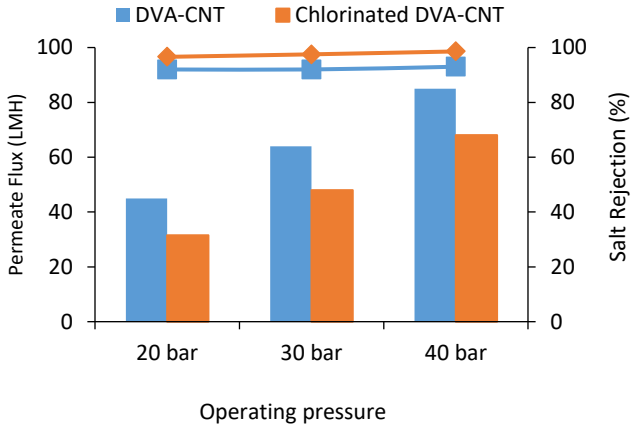

Fig. 7. Water flux and salt rejection before and after hypochlorite exposure fed with saline water (2000 ppm) at different applied pressures and room temperature (25 °C).

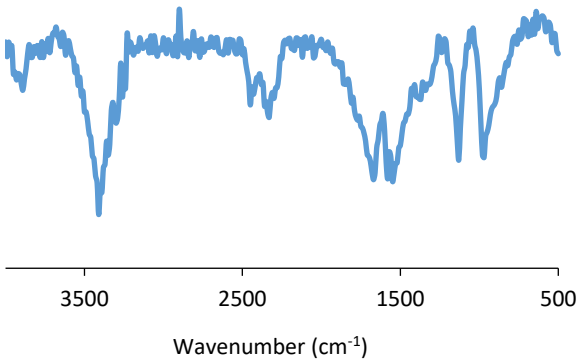

Fig. 2. FT-IR spectrum of chlorinated DVA-CNT membrane.

As shown in Figure 7, there is a modification in the salt rejection efficiency of the DVA-CNT membrane after hypochlorite contact. The carboxylic functions induced salt rejection due to electrostatic repulsion and the Donnan effect. On the other hand, the oxidation of the CNTs, especially the inner wall of the MWCNTs, resulted in some defects in the graphitic structure of the CNTs and destroyed the atomically smooth inner surface of the CNTs. Moreover, the functionalized CNTs had higher interaction with water molecules. These two phenomena caused a decrease in the permeability of the DVA-CNT membrane. However, its permeability was higher than the commercial polymeric RO membrane (BW30). By comparison, the commercial BW30 membrane can only withstand approximately 3000 ppm.h of exposure to free chlorine in its operational lifetime [97]; the DVA-CNT membrane had superior chlorine resistance.

4. Conclusions

This article presented results regarding the synthesis and characterization of a vertically aligned carbon nanotube and a two-step pyrolyzed vertically aligned carbon nanotube (DVA-CNT) membrane and its feasibility study for the desalination of salt water. The results showed that the VA-CNT membrane, prepared through template assisted pyrolysis of organic materials into the uniform pores of AAO, resulted in a porous carbon structure of vertically aligned and uniform carbon nanotubes. However, the DVA-CNT membranes had a microporous active layer that covered the surface of the AAO. The carbons nanotubes obtained by this method had a graphitic structure the same as commercial multi-walled carbon nanotubes. The DVA-CNT membranes had high antibacterial efficiency so that about 70% of the adsorbed cells were killed by the aligned CNTs, whereas the BW30 membrane's antibacterial activity was about 15 %. The adsorption of cells and subsequently CNT-cell bonding were the main mechanisms disrupting the membrane cell and resulting in their death. The performance (flux, rejection, and fouling tendency) of DVA-CNT membranes employed as a molecular sieve membrane for the desalination of saline water was compared with the commercial RO membrane (BW30). The permeability of the DVA-CNT membrane was about twofold of the permeability of the commercial RO membrane. The higher permeability of the DVA-CNT membrane resulted from the friction-less transport of water molecules into the CNTs. This flow behavior was approximately $2.3 - 2.9 \times 10^3$ times faster than the conventional flow under the no-slip condition. Additionally, the salt rejection efficiency of the DVA-CNT membrane was comparable to the commercial RO membrane. Finally, the DVA-CNT membranes revealed superior biofouling resistance, represented by an approximately 25% fewer permeate flux decline than the BW30 membrane. Also, the DVA-CNT membrane had reasonable chlorine stability under 48,000 ppm.h of chlorine exposure, demonstrating a high chemical tolerance that allowed for chemical cleaning and biofouling control techniques. The present study shows that the DVA-CNT membranes with proper performance and antibacterial and antifouling activity are appropriate candidates for water purification where reverse osmosis and/or nanofiltration membranes are indicated. But the complexity and high cost of their fabrication procedure and difficult scale-up process are obstacles to the practical application of CNT membranes in membrane separation industries.

Acknowledgements

The financial support of the Iranian Nanotechnology Initiative Council (grant no. 48260) is greatly appreciated.

References

[1] Service, R. F. (2006). Desalination freshens up, *Science*, 313, 1088-1090.

[2] Gorjian, S., Ghobadian, B. (2015). Solar desalination: A sustainable solution to water crisis in Iran. *Renewable and sustainable energy reviews*, *48*, 571-584.

[3] Anis, S. F., Hashaikeh, R., Hilal, N. (2019). Reverse osmosis pretreatment technologies and future trends: A comprehensive review. *Desalination*, *452*, 159-195.

[4] Elimelech, M., Phillip, W. A. (2011). The future of seawater desalination: energy, technology, and the environment. *Science*, *333*(6043), 712-717.

[5] Semiat, R. (2008). Energy issues in desalination processes. *Environmental science and technology*, *42*(22), 8193-8201.

[6] Shafi, H. Z., Matin, A., Khan, Z., Khalil, A., Gleason, K. K. (2015). Surface modification of reverse osmosis membranes with zwitterionic coatings: a potential strategy for control of biofouling. *Surface and coatings technology*, *279*, 171-179.

[7] Sheikholeslami, R. (2007). Fouling in membranes and thermal units. *1st edition, L'Aquila: Bala-ban Desalination Publications*.

[8] Potts, D. E., Ahlert, R. C., Wang, S. S. (1981). A critical review of fouling of reverse osmosis membranes. *Desalination*, *36*(3), 235-264.

[9] Zhao, F., Xu, K., Ren, H., Ding, L., Geng, J., hang, Y. (2015). Combined effects of organic matter and calcium on biofouling of nanofiltration membranes. *Journal of membrane science*, *486*, 177-188.

[10] Macedonio, F., Drioli, E., Gusev, A. A., Bardow, A., Semiat, R., Kurihara, M. (2012). Efficient technologies for worldwide clean water supply. *Chemical engineering and processing: Process intensification*, *51*, 2-17.

[11] Greenlee, L. F., Lawler, D. F., Freeman, B. D., Marrot, B., Moulin, P. (2009). Reverse osmosis desalination: water sources, technology, and today's challenges. *Water research*, *43*(9), 2317-2348.

[12] Geise, G. M., Park, H. B., Sagle, A. C., Freeman, B. D., McGrath, J. E. (2011). Water permeability and water/salt selectivity tradeoff in polymers for desalination. *Journal of membrane science*, *369*(1-2), 130-138.

[13] Ma, T., Su, Y., Li, Y., Zhang, R., Liu, Y., He, M., Jiang, Z. (2016). Fabrication of electro-neutral nanofiltration membranes at neutral pH with antifouling surface via interfacial polymerization from a novel zwitterionic amine monomer. *Journal of membrane science*, *503*, 101-109.

[14] Rana, D., Matsuura, T. (2010). Surface modifications for antifouling membranes. *Chemical reviews*, *110*(4), 2448-2471.

[15] Yang, H. L., Chun-Te Lin, J., Huang, C. (2009). Application of nanosilver surface modification to RO membrane and spacer for mitigating biofouling in seawater desalination. *Water research*, *43*(15), 3777-3786.

[16] Li, Q., Mahendra, S., Lyon, D. Y., Brunet, L., Liga, M. V., Li, D., Alvarez, P. J. (2008). Antimicrobial nanomaterials for water disinfection and microbial control: potential applications and implications. *Water research*, *42*(18), 4591-4602.

[17] Park, S. H., Kim, S. H., Park, S. J., Ryoo, S., Woo, K., Lee, J. S., Lee, J. H. (2016). Direct incorporation of silver nanoparticles onto thin-film composite membranes via arc plasma deposition for enhanced antibacterial and permeation performance. *Journal of membrane science*, *513*, 226-235.

[18] D. Mamadou, J.S. Duncan, N. Savage, A. Street, R.C. Sustich, Nanotechnology applications for clean water, 1 st ed., William Andrew publishing, New York, 2008.

[19] Goh, P. S., Ismail, A. F., Hilal, N. (2016). Nano-enabled membranes technology: sustainable and revolutionary solutions for membrane desalination?. *Desalination*, *380*, 100-104.

[20] Saleem, H., Zaidi, S. J. (2020). Nanoparticles in reverse osmosis membranes for desalination: A state of the art review. *Desalination*, *475*, 114171.

[21] Kar, S., Bindal, R. C., Tewari, P. K. (2012). Carbon nanotube membranes for desalination and water purification: Challenges and opportunities. *Nano today*, *7*(5), 385-389.

[22] Ahn, C. H., Baek, Y., Lee, C., Kim, S. O., Kim, S., Lee, S., Yoon, J. (2012). Carbon nanotube-based membranes: Fabrication and application to desalination. *Journal of industrial and engineering chemistry*, *18*(5), 1551-1559.

[23] Hinds, B. J., Chopra, N., Rantell, T., Andrews, R., Gavalas, V., Bachas, L. G. (2004). Aligned multiwalled carbon nanotube membranes. *Science*, *303*(5654), 62-65.

[24] Majumder, M., Chopra, N., Andrews, R., Hinds, B. J. (2005). Enhanced flow in carbon nanotubes. *Nature*, *438*(7064), 44-44.

[25] Holt, J. K., Park, H. G., Wang, Y., Stadermann, M., Artyukhin, A. B., Grigoropoulos, C. P., Bakajin, O. (2006). Fast mass transport through sub-2-nanometer carbon nanotubes. *Science*, *312*(5776), 1034-1037.

[26] Corry, B. (2008). Designing carbon nanotube membranes for efficient water desalination. *The journal of physical chemistry B*, *112*(5), 1427-1434.

[27] Corry, B. (2011). Water and ion transport through functionalised carbon nanotubes: implications for desalination technology. *Energy and environmental science*, *4*(3), 751-759.

[28] Gourary, B. S., Adrian, F. J. (1960). Wave functions for electron-excess color centers in alkali halide crystals. In *solid state physics* (Vol. 10, pp. 127-247). Academic press.

[29] Conway, B. E. (1981). Ionic hydration in chemistry and biophysics.

[30] Lee, W., Ji, R., Gösele, U., Nielsch, K. (2006). Fast fabrication of long-range ordered porous alumina membranes by hard anodization. *Nature materials*, *5*(9), 741-747.

[31] H. Azami , M.R. Omidkhah, Synthesis of anti-biofouling vertically aligned carbon nanotube membrane for ultrafiltration, in: The 12th international conference on membrane science and technology (MST2015), Tehran, Iran, 2015.

[32] Sarbolouki, M. N., Miller, I. F. (1973). On pore flow models for reverse osmosis desalination. *Desalination*, *12*(3), 343-359.

[33] Pappenheimer, J. R., Renkin, E. M., Borrero, L. M. (1951). Filtration, diffusion and molecular sieving through peripheral capillary membranes: a contribution to the pore theory of capillary permeability. *American journal of physiology-legacy content*, *167*(1), 13-46.

[34] Ferry, J. D. (1936). Statistical evaluation of sieve constants in ultrafiltration. *The journal of general physiology*, *20*(1), 95-104.

[35] Renkin, E. M. (1954). Filtration, diffusion, and molecular sieving through porous cellulose

membranes. *The journal of general physiology*, *38*(2), 225-243.

[36] Wei, X., Wang, Z., Zhang, Z., Wang, J., Wang, S. (2010). Surface modification of commercial aromatic polyamide reverse osmosis membranes by graft polymerization of 3-allyl-5, 5-dimethylhydantoin, *Journal of membrane science*, *351*(1-2), 222-233.

[37] Xu, J., Wang, Z., Yu, L., Wang, J., Wang, S. (2013). A novel reverse osmosis membrane with regenerable anti-biofouling and chlorine resistant properties. *Journal of membrane science*, *435*, 80-91.

[38] Azami, H., Omidkhah, M. R. (2017). Preparation, characterization, and application of vertically aligned CNT sheets through template assisted pyrolysis of PBI-Kapton. *The Canadian journal of chemical engineering*, *95*(2), 307-318.

[39] Cuesta, A., Dhamelincourt, P., Laureyns, J., Martinez-Alonso, A., Tascon, J. M. (1998). Comparative performance of X-ray diffraction and Raman microprobe techniques for the study of carbon materials. *Journal of materials chemistry*, *8*(12), 2875-2879.

[40] Hosseini, S. S., Omidkhah, M. R., Moghaddam, A. Z., Pirouzfar, V., Krantz, W. B., Tan, N. R. (2014). Enhancing the properties and gas separation performance of PBI–polyimides blend carbon molecular sieve membranes via optimization of the pyrolysis process. *Separation and purification technology*, *122*, 278-289.

[41] Kuncser, V., Palade, P., Kuncser, A., Greculeasa, S., Schinteie, G. (2014). Engineering magnetic properties of nanostructures via size effects and interphase interactions. In *size effects in nanostructures* (pp. 169-237). Springer, Berlin, Heidelberg.

[42] Zarbin, A. J., Bertholdo, R., Oliveira, M. A. (2002). Preparation, characterization and pyrolysis of poly (furfuryl alcohol)/porous silica glass nanocomposites: novel route to carbon template. *Carbon*, *40*(13), 2413-2422.

[43] Costa, S., Borowiak-Palen, E., Kruszynska, M., Bachmatiuk, A., Kalenczuk, R. J. (2008). Characterization of carbon nanotubes by Raman spectroscopy. *Materials science-poland*, *26*(2), 433-441.

[44] Kuzmany, H. (2014). Phonon Structures and Raman Effect of Carbon Nanotubes and Graphene. *Carbon nanotubes and graphene*, 99-149.

[45] Reich, S., Thomsen, C. (2004). Raman spectroscopy of graphite. *Philosophical transactions of the royal society of London. Series A: Mathematical, physical and engineering sciences*, *362*(1824), 2271-2288.

[46] Cuesta, A., Dhamelincourt, P., Laureyns, J., Martinez-Alonso, A., Tascón, J. D. (1994). Raman microprobe studies on carbon materials. *Carbon*, *32*(8), 1523-1532.

[47] Lotfi, R., Rashidi, A., Mohsennia, M. (2014). A rigorous comparison of methods for multi-walled carbon nanotubes purification using raman spectroscopy. *Journal of petroleum science and technology*, *4*(1), 57-62.

[48] Murphy, H., Papakonstantinou, P., Okpalugo, T. T. (2006). Raman study of multiwalled carbon nanotubes functionalized with oxygen groups. *Journal of vacuum science and technology B: Microelectronics and nanometer structures processing, measurement, and phenomena*, *24*(2), 715-720.

[49] Shu-Sen, W. (1988). Effect of solution viscosity on ultrafiltration flux. *Journal of membrane science*, *39*(2), 187-194.

[50] Mehdizadeh, H., Dickson, J. M., Eriksson, P. K. (1989). Temperature effects on the performance of thin-film composite, aromatic polyamide membranes. *Industrial and engineering chemistry research*, *28*(6), 814-824.

[51] Baek, Y., Kim, C., Seo, D. K., Kim, T., Lee, J. S., Kim, Y. H., Yoon, J. (2014). High performance and antifouling vertically aligned carbon nanotube membrane for water purification. *Journal of membrane Science*, *460*, 171-177.

[52] Sokhan, V. P., Nicholson, D., Quirke, N. (2002). Fluid flow in nanopores: Accurate boundary conditions for carbon nanotubes. *The journal of chemical physics*, *117*(18), 8531-8539.

[53] Kimura, S., Sourirajan, S. (1967). Analysis of data in reverse osmosis with porous cellulose acetate membranes used. *AIChE journal*, *13*(3), 497-503.

[54] R.W. Baker (2004), Membrane technology and applications, Second edition ed., John Wiley and Sons, Ltd., Menlo Park, California.

[55] Zhu, Y., Gupta, K. M., Liu, Q., Jiang, J., Caro, J., Huang, A. (2016). Synthesis and seawater desalination of molecular sieving zeolitic imidazolate framework membranes. *Desalination*, *385*, 75-82.

[56] Ibrahim, S. M., Xu, R., Nagasawa, H., Naka, A., Ohshita, J., Yoshioka, T., Tsuru, T. (2014). Insight into the pore tuning of triazine-based nitrogen-rich organoalkoxysilane membranes for use in water desalination. *RSC Advances*,*4*(45), 23759-23769.

[57] Matsuura, T. (1993). *Synthetic membranes and membrane separation processes*. CRC press.

[58] Tsuru, T., Miyawaki, M., Yoshioka, T., Asaeda, M. (2006). Reverse osmosis of nonaqueous solutions through porous silica-zirconia membranes. *AIChE journal*, *52*(2), 522-531.

[59] Zhu, B., Hong, Z., Milne, N., Doherty, C. M., Zou, L., Lin, Y. S., Duke, M. (2014). Desalination of seawater ion complexes by MFI-type zeolite membranes: temperature and long term stability. *Journal of membrane science*, *453*, 126-135.

[60] Xu, R., Wang, J., Kanezashi, M., Yoshioka, T., Tsuru, T. (2013). Reverse osmosis performance of organosilica membranes and comparison with the pervaporation

and gas permeation properties. *AIChE Journal*, *59*(4), 1298-1307.

[61] Gierer, A., Wirtz, K. (1953). Molecular theory of microfriction. *Z. Naturforsch. A*, *8*, 532-538.

[62] von Recum, A. F. (Ed.). (1998). *Handbook of biomaterials evaluation: scientific, technical and clinical testing of implant materials*. CRC Press.

[63] Thomas, M., Corry, B., Hilder, T. A. (2014). What have we learnt about the mechanisms of rapid water transport, ion rejection and selectivity in nanopores from molecular simulation?. *Small*, *10*(8), 1453-1465.

[64] Hinds, B. (2012). Dramatic transport properties of carbon nanotube membranes for a robust protein channel mimetic platform. *Current opinion in solid state and materials science*, *16*(1), 1-9.

[65] Hirunpinyopas, W. (2019). *Electrochemical applications for two-dimensional (2D) Materials: Self-assembly at liquid| liquid interfaces and assembled 2D material laminates*. The university of manchester (United Kingdom), pp 640.

[66] Gong, X., Li, J., Xu, K., Wang, J., Yang, H. (2010). A controllable molecular sieve for Na+ and K+ ions. *Journal of the American chemical society*, *132*(6), 1873-1877.

[67] Peter, C., Hummer, G. (2005). Ion transport through membrane-spanning nanopores studied by molecular dynamics simulations and continuum electrostatics calculations. *Biophysical journal*, *89*(4), 2222-2234.

[68] Peter, C., Hummer, G. (2005). Ion transport through membrane-spanning nanopores studied by molecular dynamics simulations and continuum electrostatics calculations. *Biophysical journal*, *89*(4), 2222-2234.

[69] Lin, J., Murad, S. (2001). A computer simulation study of the separation of aqueous solutions using thin zeolite membranes. *Molecular physics*, *99*(14), 1175-1181.

[70] Park, J. H., Sinnott, S. B., Aluru, N. R. (2006). Ion separation using a Y-junction carbon nanotube. *Nanotechnology*, *17*(3), 895.

[71] Balcajin, O., Noy, A., Fornasiero, F., Grigoropoulos, C. P., Holt, J. K., In, J. B., Park, H. G. (2009). Nanofluidic carbon nanotube membranes: applications for water purification and desalination. In *nanotechnology applications for clean water* (pp. 77-93). William Andrew Publishing.

[72] Song, C., Corry, B. (2009). Intrinsic ion selectivity of narrow hydrophobic pores. *The Journal of physical chemistry B*, *113*(21), 7642-7649.

[73] Kalra, A., Garde, S., Hummer, G. (2003). Osmotic water transport through carbon nanotube membranes. *Proceedings of the national academy of sciences*, *100*(18), 10175-10180.

[74] Corry, B. (2011). Water and ion transport through functionalised carbon nanotubes: implications for desalination technology. *Energy and environmental science*, *4*(3), 751-759.

[75] Mauter, M. S., Elimelech, M. (2008). Environmental applications of carbon-based nanomaterials. *Environmental science and technology, 42*(16), 5843-5859.

[76] Hummer, G., Rasaiah, J. C., Noworyta, J. P. (2001). Water conduction through the hydrophobic channel of a carbon nanotube. *Nature*, *414*(6860), 188-190.

[77] Ye, H., Zhang, H., Zhang, Z., Zheng, Y. (2011). Size and temperature effects on the viscosity of water inside carbon nanotubes. *Nanoscale research letters*, *6*(1), 1-5.

[78] Whitby, M., Quirke, N. (2007). Fluid flow in carbon nanotubes and nanopipes. *Nature nanotechnology*, *2*(2), 87-94.

[79] Joseph, S., Aluru, N. R. (2008). Why are carbon nanotubes fast transporters of water? *Nano letters*, *8*(2), 452-458.

[80] Pascal, T. A., Goddard, W. A., Jung, Y. (2011). Entropy and the driving force for the filling of carbon nanotubes with water. *Proceedings of the national academy of* sciences, 108(29), 11794-11798.

[81] M. Majumder, B. Corry, (2011) Anomalous decline of water transport in covalently modified carbon nanotube membranes, *Chemical communication*, 47 (2011) 7683–7685.

[82] Song, K., Gao, A., Cheng, X., Xie, K. (2015). Preparation of the superhydrophobic nano-hybrid membrane containing carbon nanotube based on chitosan and its antibacterial activity. *Carbohydrate polymers*, *130*, 381-387.

[83] Dizaj, S. M., Mennati, A., Jafari, S., Khezri, K., Adibkia, K. (2015). Antimicrobial activity of carbon-based nanoparticles. *Advanced pharmaceutical bulletin*, *5*(1), 19.

[84] Song, K., Gao, A., Cheng, X., Xie, K. (2015). Preparation of the superhydrophobic nano-hybrid membrane containing carbon nanotube based on chitosan and its antibacterial activity. *Carbohydrate polymers*, *130*, 381-387.

[85] Kang, S., Herzberg, M., Rodrigues, D. F., Elimelech, M. (2008). Antibacterial effects of carbon nanotubes: size does matter! *Langmuir*, *24*(13), 6409-6413.

[86] Tangpasuthadol, V., Pongchaisirikul, N., Hoven, V. P. (2003). Surface modification of chitosan films: Effects of hydrophobicity on protein adsorption. *Carbohydrate research*, *338*(9), 937-942.

[87] Al-Jumaili, A., Alancherry, S., Bazaka, K., Jacob, Mohan V. (2017). Review on the Antimicrobial Properties of Carbon Nanostructures. *Materials*, 10(9), 1-26.

[88] Mansouri, J., Harrisson, S., Chen, V. (2010). Strategies for controlling biofouling in membrane filtration systems: challenges and opportunities. *Journal of materials chemistry*, *20*(22), 4567-4586.

[89] Matin, A., Khan, Z., Zaidi, S. M. J., Boyce, M. C. (2011). Biofouling in reverse osmosis membranes for seawater desalination: phenomena and prevention. *Desalination*, *281*, 1-16.

[90] Cadotte, J. E., Petersen, R. J., Larson, R. E., Erickson, E. E. (1980). A new thin-film composite seawater reverse osmosis membrane. *Desalination*, *32*, 25-31.

[91] Bai, Y., Park, I. S., Lee, S. J., Wen, P. S., Bae, T. S., Lee, M. H. (2012). Effect of AOT-assisted multi-walled carbon nanotubes on antibacterial activity. *Colloids and surfaces B: Biointerfaces*, *89*, 101-107.

[92] Liu, S., Wei, L., Hao, L., Fang, N., Chang, M. W., Xu, R., Chen, Y. (2009). Sharper and faster "nano darts" kill more bacteria: a study of antibacterial activity of individually dispersed pristine single-walled carbon nanotube. *ACS nano*, *3*(12), 3891-3902.

[93] Kang, S., Mauter, M. S., Elimelech, M. (2008). Physicochemical determinants of multiwalled carbon nanotube bacterial cytotoxicity. *Environmental science and technology*, *42*(19), 7528-7534.

[94] Celik, E., Park, H., Choi, H., Choi, H. (2011). Carbon nanotube blended polyethersulfone membranes for fouling control in water treatment. *Water research*, *45*(1), 274-282.

[95] Ajmani, G. S., Goodwin, D., Marsh, K., Fairbrother, D. H., Schwab, K. J., Jacangelo, J. G., Huang, H. (2012). Modification of low pressure membranes with carbon nanotube layers for fouling control. *Water research*, *46*(17), 5645-5654.

[96] S.P. Chesters, N. Pena, S. Gallego, M. Fazel, M.W. Armstrong, F. del Vigo, (2011), Results from 99 sea water reverse osmosis (SWRO) membrane autopsies, in: IDA World Congress, Perth, Western Australia, pp. 1-10.

[97] Ni, L., Meng, J., Li, X., Zhang, Y. (2014). Surface coating on the polyamide TFC RO membrane for chlorine resistance and antifouling performance improvement. *Journal of membrane science*, *451*, 205-215.

[98] Glater, J., Hong, S. K., Elimelech, M. (1994). The search for a chlorine-resistant reverse osmosis membrane. *Desalination*, *95*(3), 325-345.

[99] Li, H., Yu, P., Li, H., Luo, Y. (2015). The chlorination and chlorine resistance modification of composite polyamide membrane. *Journal of applied polymer science*, *132*(10), 41584.

[100] Yang, J. C., Yen, C. H., Wang, W. J., Horng, J. J., Tsai, Y. P. (2010). Assessment of adequate sodium hypochlorite concentration for pre-oxidization of multi-walled carbon nanotubes. *Journal of chemical technology and biotechnology*, *85*(5), 699-707.

[101] Skarzewski, J., Siedlecka, R. (1992). Synthetic oxidations with hypochlorites. A review. *Organic preparations and procedures international*, *24*(6), 623-647.

[102] Liu, W., Zhang, J., Cheng, C., Tian, G., Zhang, C. (2011). Ultrasonic-assisted sodium hypochlorite oxidation of activated carbons for enhanced removal of Co (II) from aqueous solutions. *Chemical engineering journal*, *175*, 24-32.

[103] Ismail, A. F., Rana, D., Matsuura, T., Foley, H. C. (2011). *Carbon-based membranes for separation processes*. Springer science and business media.